COMPRESSED AIR-FLOW AND PHYSICAL PROPERTY IN MINE TUNNELS DURING CYCLIC CHARGING AND DISCHARGING

by

Cheng-Zheng CAI*, Zheng-Chao ZHU, Zeng-Xin ZOU*, Bo WANG, Jia-Cheng LI, and Yue-Jin ZHOU

State Key Laboratory of Intelligent Construction and Healthy Operation and Maintenance of Deep Underground Engineering,
School of Low-Carbon Energy and Power Engineering,
China University of Mining and Technology, Xuzhou, China

Original scientific paper
https://doi.org/10.2298/TSCI2502145C

This paper utilizes CFD methods to simulate high pressure gas charging and discharging in a horseshoe-shaped tunnel. Simulation results reveal linear pressure and temperature variations during charging and discharging cycles, with stabilized trends after several cycles. The evolution of air physical properties such as density, viscosity, thermal conductivity, and specific heat capacity within the tunnel is also analyzed. The air density increases with pressure and decreases with temperature, stabilizing after several cycles. Viscosity and thermal conductivity exhibit similar trends to temperature, with minor variations throughout the cycle. Specific heat capacity increases during gas charging, remains constant during storage, and decreases during gas release. The study contributes to the optimization of CAES systems in abandoned coal mines by providing detailed insights into air-flow and heat transfer characteristics.

Key words: *compressed air, energy storage, flow and heat transfer, physical property*

Introduction

The global energy sector aims to develop a green, low carbon, and efficient system, with hydroelectric, wind, and photovoltaic power as main clean energy sources. Yet, wind and photovoltaic power face volatility and randomness issues, hindering large-scale use [1, 2]. Compressed air energy storage (CAES) emerges as a solution, compressing air during low grid loads and releasing it during highs to stabilize the grid [3]. Abandoned coal mines provide ample underground space for CAES. Accurate thermodynamic predictions during charging, discharging, and storage are crucial for evaluating underground caverns. Researchers have developed models to study cavern operations, advancing CAES theory, especially for unlined rock caverns [4-7].

Despite progress, there is still a lack of understanding of air-flow states and physical property evolution within the air storage chamber. To address this, CFD methods were used to simulate high pressure gas charging and discharging in an unlined horseshoe-shaped tunnel. The research revealed pressure and temperature variations, analyzed flow field states and heat transfer characteristics, and summarized physical property trends. These findings provide theoretical support for optimizing CAES systems.

* Corresponding authors, e-mails: caicz@cumt.edu.cn; 386025214@qq.com

Numerical model

Geometric model and boundary conditions

The study focused on the high pressure air charging, storage, and discharging process with simulated large mass-flow. As shown in fig. 1, the model comprised two parts: a 50 m long tunnel with a horseshoe-shaped section (1.5 m semi-circular arc roof, 3 m × 1.5 m rectangular base, 8.034 m² area, 401.71 m³ volume) surrounded by 1 m thick unlined rock. Initial tunnel pressure was pre-set before operations. The flow field inlet, set as a mass-flow boundary with initial gauge pressure matching the tunnel's, served as both inlet during charging and outlet during discharging. Mass-flow adjustments facilitated transitions between stages. The air-rock contact was interfaced, other boundaries were walled. Local mesh refinement densified fluid and fluid-solid interfaces. During charging, air entered and compressed within the tunnel.

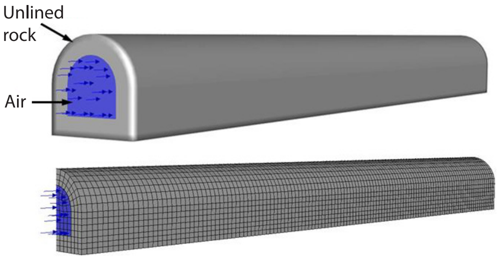

Figure 1. Numerical model of air charging and discharging in the tunnel

Mathematical model

The governing equations for fluid control consisted of the continuity equation, the momentum equation, and the energy equation. Among them, the continuity equation was given [8]:

$$\frac{\partial \rho}{\partial t}+\frac{\partial(\rho u_1)}{\partial x_1}+\frac{\partial(\rho u_2)}{\partial x_2}+\frac{\partial(\rho u_3)}{\partial x_3}=S_m \tag{1}$$

where ρ is the density of the fluid, t – the flow time, u_1, u_2, u_3 are the velocities along the three directions of the co-ordinate system, x_1, x_2, x_3 – the co-ordinate distances along the three directions of the co-ordinate system, and S_m – the increase in the mass of the continuous phase caused by the discrete phase.

The momentum equation is presented [8]:

$$\frac{\partial}{\partial t}(\rho u_i)+\frac{\partial}{\partial x_j}(\rho u_i u_j)=-\frac{\partial p}{\partial x_i}+\frac{\partial \tau_{ij}}{\partial x_j}+\rho \mathrm{g}_i+F_i \tag{2}$$

$$\tau_{ij}=\mu\left[\left(\frac{\partial u_i}{\partial x_j}+\frac{\partial u_j}{\partial x_i}\right)-\frac{2}{3}\frac{\partial u_l}{\partial x_l}\delta_{ij}\right] \tag{3}$$

$$\delta_{ij}=\begin{cases}0(i=j)\\1(i\neq j)\end{cases} \tag{4}$$

where p is the pressure of the fluid, τ_{ij} – the deviatoric stress tensor, ρ_{gi} – the body force due to gravity, F_i – the body force per unit volume, μ – the molecular viscosity, and δ_{ij} – the Kronecker delta symbol.

The energy equation is presented [8]:

$$\frac{\partial}{\partial t}(\rho E)+\frac{\partial}{\partial x_i}\left[u_i(\rho E+p)\right]=\frac{\partial}{\partial x_i}\left[\frac{k_{\mathrm{eff}}}{c_p}\frac{\partial T}{\partial x_i}-\sum_{j'}h_{j'}J_{j'}+u_j(\tau_{ij})_{\mathrm{eff}}\right]+S_h \tag{5}$$

where E is the internal energy of the fluid, k_{eff} – the effective thermal conductivity, T [K] – the temperature, $h_{j'}$ – the enthalpy, $J_{j'}$ – the diffusion flux, and S_h – the volumetric heat source.

Heat transfer model for rock

The focus of this paper was on the flow and heat transfer laws in compressed air energy storage within elongated tunnels. Consequently, the mechanical behavior of the surrounding rock was disregarded, considering only the heat transfer between it and the high pressure air. The heat conduction equation in the rock was [9]:

$$\rho_s c_s \frac{\partial T_s}{\partial t} = \nabla(\Lambda_s \nabla T_s) \tag{6}$$

where ρ_s is the density of the surrounding rock, c_s – the specific heat capacity of the surrounding rock at constant volume, Λ_s – the thermal conductivity, which was also equal to the product of the thermal diffusivity k_s, specific heat capacity c_s, and density ρ_s.

Air physical property model

Drawing on Zhou *et al.* [10] and Zhang *et al.* [11], the compressibility factor Z was computed using Berthelot's gas equation of state. Air was modeled as a real gas with uniformly distributed density, enabling the determination of pressure at any instance in the compressed air energy storage process:

$$p_a = \left(\frac{\mathrm{R}}{V}\right) Z m T_a \tag{7}$$

$$Z = 1 - \frac{9}{128}\left(\frac{p_a}{p_c}\right)\left(\frac{T_c}{T}\right)\left(\frac{6T_c}{T^2} - 1\right) \tag{8}$$

where T_c is the air critical temperature and p_c – the air critical pressure, which were 132.65 K and 3.76 MPa, respectively.

The transport property equation by Lemmon *et al.* [12], using temperature and density, was adopted. Based on this equation, the viscosity and thermal conductivity of air could be obtained.

Solving procedure

The simulation was conducted in FLUENT's pressure-based solver, coupling equations for mass, momentum, energy, and heat conductivity to simulate flow and heat transfer. Air properties were updated based on pressure and temperature. Rock-related equations were solved at each time step. Gravity (9.81 m/s^2) was included, acting negatively. Fluid-solid interfaces were set as conjugated boundary conditions, employing the conjugate heat transfer method. Table 1 displayed the simulation parameters.

Table 1. Stimulation parameters

Parameter	Tunnel length [m]	Gas storage chamber surface area [m^2]	Gas storage chamber volume [m^3]	Charging temperature [K]	Initial temperature [K]
Value	50	535.62	401.71	310	300
Parameter	Mass-flow rate of charging [kgs^{-1}]	Mass-flow rate of discharging [kgs^{-1}]	Density of surrounding rock [kgm^{-3}]	Thermal conductivity of surrounding rock [J^{-1}s^{-1}K^{-1}]	Specific heat of surrounding rock [Jkg^{-1}K^{-1}]
Value	50	75	2500	3	800

Dynamic characteristics of temperature and pressure during compressed air charging and discharging cycles

This study, grounded in practical engineering, set the initial tunnel pressure at standard atmospheric and conducted compressed air energy storage simulations. Ten working cycles were modeled within a 5-8 MPa pressure range, maintaining consistent air storage durations post-charging/discharging. Figures 2 and 3 reveal linear pressure variation during charging (peaking at 8 MPa) and discharging (dropping to 5 MPa), with minor (<0.1 MPa) fluctuations during storage. From the second cycle, pressure stabilized within the 5-8 MPa range, showing consistent changes across cycles. Regarding temperature, the first cycle saw significant variation, peaking at 420 K (a 120% increase) at 8 MPa. Subsequent cycles stabilized, with temperatures oscillating between 330 K post-charging and 289 K post-discharging. Charging caused temperature rise due to external air work, slowing as internal air volume increased. Discharging led to linear temperature decrease. The first cycle exhibited extreme temperature shifts and notable cooling during high pressure storage. As cycles progressed, temperature fluctuations diminished, stabilizing after the seventh cycle.

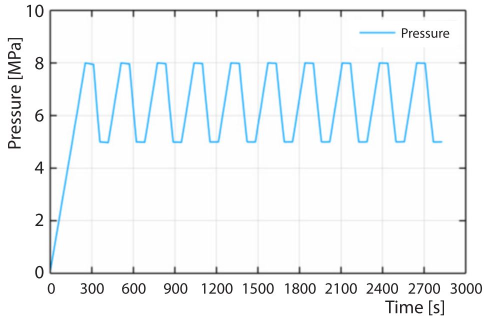

Figure 2. Pressure distribution curve

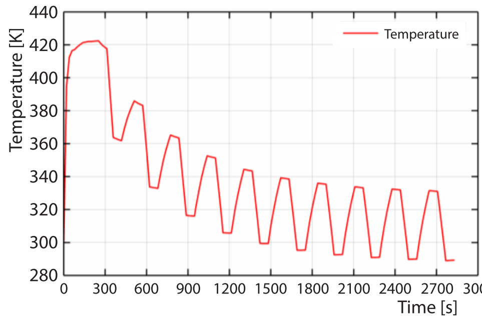

Figure 3. Temperature distribution curve

Evolution of air physical properties

Compressed air density

Air's compressibility makes its density susceptible to temperature and pressure variations during energy storage, causing fluctuations. As depicted in fig. 3, density rises with pressure and falls with temperature. Starting from the first cycle, air density showed an upward trend, reaching 65.54 kg/m³ at the end of the first charging phase and 83.45 kg/m³ by the seventh cycle. After the seventh cycle, temperature and pressure stabilized, leading to steady density variations. The average densities at the end of charging and discharging were 83.45 kg/m³ and 61.5 kg/m³, respectively. Density varied inversely with temperature, as shown in figs. 2-7, the first cycle saw significant temperature changes and lower density at higher temperatures. With more cycles and constant working pressure, temperature fluctuations decreased and stabilized, while density increased as temperature dropped. Eventually, both working temperature and density stabilized with increasing cycle count.

Compressed air viscosity

The variation pattern of viscosity across the entire cycle exhibited similarities to that of temperature, albeit with a notable distinction. At the onset of charging, temperature swiftly rose and stabilized during high pressure gas storage. Conversely, viscosity surged rapidly during the initial charging phase, then gradually increased, peaking at $2.5 \cdot 10^{-5}$ kg/ms, fig. 4. It subsequently declined during high pressure storage and continued to decrease linearly during discharging. During the initial low pressure storage phase, viscosity decreased at a slower rate. As the number of cycles increased, the viscosity variation trend stabilized, with viscosity rising to 2.14 kg/ms during charging and falling to 1.9 kg/ms during discharging. Although viscosity fluctuations were relatively regular, their magnitude was minor, exerting no significant influence on the charging and discharging processes, fig. 5.

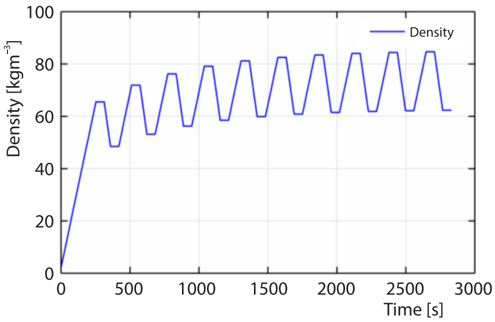

Figure 4. Density change curve

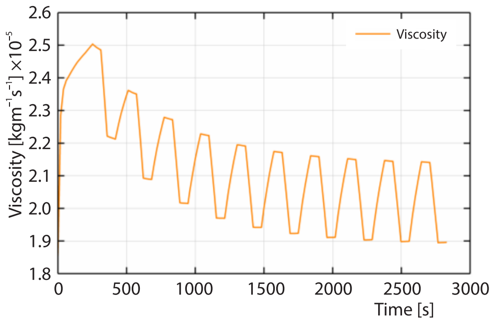

Figure 5. Viscosity change curve

Compressed air thermal conductivity

The variation pattern of the thermal conductivity during cyclic operation exhibited the same trend as that of the viscosity. As shown in fig. 6, during the initial gas charging phase of the first cycle, it rapidly increased in a short period, followed by a gradual increase, reaching a maximum of 0.00372 W/mK. Upon entering the high pressure gas storage phase, it began to decrease. During gas release, the thermal conductivity decreased linearly. During the first low pressure gas storage phase, the thermal conductivity decreased slowly. After the cyclic operation stabilized, the thermal conductivity increased linearly during gas charging, reaching a maximum of 0.0318 W/mK, and decreased linearly during gas release, reaching a minimum of 0.0277 W/mK. It remained stable during both high pressure and low pressure gas storage phases. The magnitude of the thermal conductivity variation throughout the entire operation was not significant.

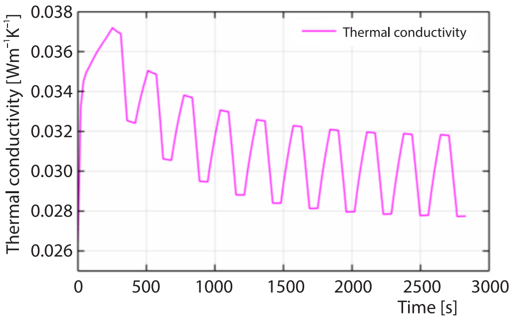

Figure 6. Thermal conductivity change curve

Compressed air specific heat

Figure 7 illustrates the specific heat capacity of air throughout the cycle, mirroring the trend of air density. It increased during gas charging, remained stable during storage, and decreased during release. Initial-

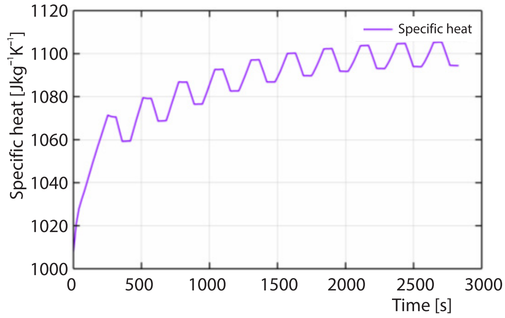

Figure 7. Air specific heat change curve

ly, it rose rapidly, then linearly, peaking at 1071.43 J/kgK during high pressure storage. During release, it decreased slowly and linearly, with a slight increase during low pressure storage. As cycles increased, variations in specific heat capacity stabilized during charging and release. During high pressure storage, it shifted from a slight decrease to a slight increase, while during low pressure storage, it transitioned from a slight increase to a slight decrease. This transition correlated with temperature changes, characterized by higher initial temperatures and lower stabilized temperatures. Consequently, the specific heat capacity during gas storage exhibited distinct characteristics before and after stabilization. When working temperature and pressure stabilized, the specific heat capacity also tended to stabilize, varying between 1094.46 J/kgK and 1105.2388 J/kgK.

Conclusion

The study utilizes computational fluid dynamics to simulate high pressure gas charging and discharging in an unlined horseshoe-shaped tunnel. It offers a comprehensive analysis of pressure, temperature, flow field, and heat transfer characteristics, as well as insights into the evolution of air properties like density, viscosity, thermal conductivity, and specific heat capacity during cyclic processes. Density increases with pressure and decreases with temperature, stabilizing after cycles. Viscosity and thermal conductivity follow temperature trends with minor variations. Specific heat capacity rises during charging, remains steady during storage, and falls during release. This research supports CAES system optimization and suggests abandoned coal mines as potential energy storage sites.

Nomenclature

c_s – specific heat capacity of rock, [Jkg^{-1}]
E – internal energy of the fluid, [Jkg^{-1}]
$h_{j'}$ – enthalpy, [Jkg^{-1}]
$J_{j'}$ – diffusion flux
k – thermal conductivity, [Wm^{-1}K^{-1}]
m – mass, [kg]
p – pressure of the fluid, [MPa]
R – gas constant, [Jmol^{-1}K^{-1}]
S_h – volumetric heat source, [Jm^{-3}s^{-1}]
T – temperature, [K]
u – velocity, [ms^{-1}]
V – olume, [MPa]
x – co-ordinate distances, [m]
Z – compressibility factor

Greek symbols

ρ – density, [kgm^{-3}]
μ – viscosity, [Pa·s]

Acknowledgment

This research was funded by the National Key R&D Program of China (Grant No. 2022YFE0129100), and Fundamental Research Funds for the Central Universities (Grant No. 2024KYJD100).

References

[1] Raju, M., *et al.*, Modelling and Simulation of Compressed Air Storage in Caverns: A Case Study of the Huntorf Plant, *Applied Energy*, *89* (2012), 1, pp. 474-481
[2] Facci, A. L., *et al.*, Trigenerative Micro Compressed Air Energy Storage: Concept and Thermodynamic Assessment, *Applied Energy*, *158* (2015), 2, pp. 243-254
[3] He, Y., *et al.*, Compression Performance Optimization Considering Variable Charge Pressure in an Adiabatic Compressed Air Energy Storage System, *Energy*, *165* (2018), 2, pp. 349-359
[4] Xia, C., *et al.* A Simplified and Unified Analytical Solution for Temperature and Pressure Variations in Compressed Air Energy Storage Caverns, *Renewable Energy*, *74* (2015), 4, pp. 718-726
[5] Zhang, Y., *et al.*, The Thermodynamic Effect of Air Storage Chamber Model on Advanced Adiabatic Compressed Air Energy Storage System, *Renewable Energy*, *57* (2013), 3, pp. 469-478
[6] Kushnir, R., *et al.*, Temperature and Pressure Variations within Compressed Air Energy Storage Caverns, *International Journal of Heat and Mass Transfer*, *55* (2012), 21-22, pp. 5616-5630

[7] Guo, C., *et al*., Modelling Studies for Influence Factors of Gas Bubble in Compressed Air Energy Storage in Aquifers, *Energy*, *107* (2016), 2, pp. 48-59
[8] Batchelor, G. K., *An Introduction Fluid Dynamics*, Cambridge University Press, Cambridge, UK, 2000
[9] Cai, C., *et a*l, Downhole Heterogeneous Heat Transfer Characteristics and Rock Stress Distributions Induced by Liquid Nitrogen Jet, *Thermal Science*, *28* (2024), 4B, pp. 3429-3434
[10] Zhou, S., *et al*., An Analytical Solution for Mechanical Responses Induced by Temperature and Air Pressure in a Lined Rock Cavern for Underground Compressed Air Energy Storage, *Rock Mechanics and Rock Engineering*, *48* (2015), 2, pp. 749-770
[11] Zhang, G., *et al*., Stability and Tightness Evaluation of Bedded Rock Salt Formations for Underground Gas/Oil Storage, *Acta Geotechnica*, *9* (2014), 1, pp. 161-179
[12] Lemmon, E. W., *et al*., Viscosity and Thermal Conductivity Equations for Nitrogen, Oxygen, Argon, and Air, *International Journal of Thermophysics*, *25* (2004), 1, pp. 21-69

Paper submitted: October 22, 2024
Paper revised: November 25, 2024
Paper accepted: December 12, 2024